Sixth International Symposium on Turbulence and Shear Flow Phenomena
Seoul, Korea, 22-24 June 2009

DIRECT NUMERICAL SIMULATION OF A MODEL ESTUARY

Rolf Henniger, Leonhard Kleiser
Institute of Fluid Dynamics
ETH Zürich
Sonneggstrasse 3, 8092 Zurich, Switzerland
henniger@ifd.mavt.ethz.ch, kleiser@ifd.mavt.ethz.ch

Eckart Meiburg
Department of Mechanical Engineering
University of California at Santa Barbara
Santa Barbara, CA 93106, USA
meiburg@engineering.ucsb.edu

ABSTRACT

We investigate numerically the mixing of freshwater with ambient brine in a laboratory-scale estuary, along with associated particle settling processes. We first discuss and specify a numerical setup which takes the most important features into account, such that our configuration is relatively close to reality and employs correspondingly only little modeling. The flow is studied in a spatial framework in order to gain a statistically stationary solution which also provides time-averaged results. The analysis of the computational results is divided into two parts: first we investigate different aspects of the freshwater/saltwater interaction, and second we take a closer look at the transport of suspended particles as well as their settling to the ground. Particularly, we find a qualitatively good agreement of the particle settling mechanisms with laboratory experiments.

INTRODUCTION

The details of freshwater mixing with ambient brine in estuaries as well as the transport of suspended particles to the ocean are still not fully understood. Especially the transport mechanisms of natural sediment and pollutants are of interest since up to ten billion metric tons of sediment are transported annually by rivers to continental shelves. This is of great importance for the marine environment. In most cases, the particle-freshwater mixture is still lighter than the saltwater near the estuaries, such that the river plumes are positively buoyant.

Also the understanding of the processes that remove sediment from the base of such surface plumes is incomplete. The settling process of the suspended particles is controversial in the literature; the only agreement is that Stokes settling of disaggregated constituent grains cannot account for the sediment flux out of typical river plumes. The most popular assumption for an enhanced particle settling is the *flocculation* of individual particles since larger effective aggregate diameters lead to larger Stokes settling speeds. Other authors favor the positive influence of *turbulence* on the effective particle settling speed which can be increased by up to 10-50% compared to Stokes settling.

The goal of the present study is to establish an appropriate numerical setup which allows a better understanding of sediment removal from such stratified shear layers in the presence of turbulence as well as the interaction between particles and turbulence. Similar practical experiments have been conducted in the past for instance by Maxworthy (1999), Parsons *et al.* (2001) and McCool and Parsons (2004). These experiments are restricted by a couple of practical limitations which we try to overcome by our numerical simulation setup. Our aim is to study a more or less realistic scenario which is intended to be closer to reality. However, genuine river flows are still out of reach of highly accurate and reliable numerical simulations and we can focus only on an laboratory-scale problem. We consider only density variations due to salinity and suspended particles which are both modeled in an Eulerian framework, such that an additional transport equation for each concentration is integrated in time.

GOVERNING EQUATIONS

We describe all density variations of the fluid phase in an Eulerian manner by means of concentrations which lead to additional volumetric forces on the carrier fluid. The nondimensional transport equation for each of the concentrations c_k $(k = 1, 2)$ reads

$$\frac{\partial c_k}{\partial t} + \left(\left(u + u_k^{\mathrm{s}} e^{\mathrm{g}}\right) \cdot \nabla\right) c_k = \frac{1}{Re\, Sc_k} \Delta c_k \tag{1}$$

with Re as the Reynolds number, Sc_k as the Schmidt numbers, u as the fluid velocity, u_k^{s} as scalar particle settling velocities and $-e^{\mathrm{g}}$ as the unity vector in gravity direction. As described later, all relative density variations will be below two percent such that the Boussinesq approximation can be applied at tolerable error. Using this model, the dimensionless incompressible Navier–Stokes equations read

$$\frac{\partial u}{\partial t} + (u \cdot \nabla)\, u \;=\; -\nabla p + \frac{1}{Re} \Delta u + e^{\mathrm{g}} \sum_k Ri_k c_k \tag{2a}$$

$$\nabla \cdot u \;=\; 0 \tag{2b}$$

where Ri_k are the Richardson numbers as a measure of the potential energy compared to the kinetic energy in the flow. Both, Re and Ri_k, will be defined below. We neglect in this configuration the influence of Coriolis forces which are of great importance for large-scale estuaries. For Eq. (1) and (2) we employ either Dirichlet boundary conditions

$$c = c_0, \qquad u = u_0 \tag{3}$$

or convective and no-flux boundary conditions, respectively,

$$\frac{\partial c}{\partial t} + U_n^{\mathrm{g}} \frac{\partial c}{\partial n} = 0 \;\text{ for }\; U_n^{\mathrm{g}} > 0 \tag{4a}$$

$$U_n^{\mathrm{g}} c - \frac{1}{Re\,Sc}\frac{\partial c}{\partial n} = 0 \;\text{ for }\; U_n^{\mathrm{g}} \leq 0 \tag{4b}$$

$$\frac{\partial u}{\partial t} + U_n \frac{\partial u}{\partial n} = 0 \tag{4c}$$

with n as the boundary-normal direction. The convection velocities $U_n^{\mathrm{g}} = n \cdot (u + u^{\mathrm{s}} e^{\mathrm{g}})$ and U_n have to be specified. We will discuss the application of the different boundary conditions on the configuration below in more detail.

NUMERICAL APPROACH

Eq. (1) and (2) with boundary conditions (3) or (4) are discretized in time and space for a numerical solution. If the viscous time-step limit is more restrictive than the convective one, the diffusive terms are treated implicitly in time with the Crank–Nicolson scheme. Otherwise, a low-storage, third-order accurate Runge–Kutta integration scheme is employed as for all other terms in Eq. (1) and (2a). Explicit, sixth-order accurate finite differences on staggered grids are chosen for the spatial discretization. Only the convective terms are discretized with fifth-order upwind-biased finite differences since our grid will not be fine enough to fully resolve the dissipative turbulent scales and also no sub-grid scale model will be employed. To maintain at least second-order accuracy in time for the Crank-Nicholson scheme, each sub-time step requires a solution of the resulting coupled linear system of equations for the velocity, pressure and concentrations. The solution is found iteratively in a SIMPLE-type fashion, i.e. by solving a Schur complement problem for the pressure. The linear systems of equations within the preconditioner are of Poisson type and are solved with the Krylov subspace method BiCGstab combined with a geometric multigrid preconditioner. All Helmholtz equations can be solved directly with BiCGstab due to their better conditioning. More details on the algorithm and the implementation are described in Henniger *et al.* (2007,2009).

FLOW CONFIGURATION

The simulation setup for an idealized estuary mouth is depicted in Figure 1. We use a rectangular box with the extents $\widetilde{L}_1 \times \widetilde{L}_2 \times \widetilde{L}_3$ which has an inflow 'I' and an outflow boundary 'O'. The heavier saltwater (index $k = 1$) is typically located in the lower part of the domain. Because (in our parameter range) the freshwater is lifted above the brine in the vicinity of the estuary mouth before the mixing process takes place, we feed it continuously into the domain in a small section of the upper part of 'I'. At some later time, the freshwater carries with it also suspended particles (index $k = 2$). The reference quantities for the simulation are the freshwater inflow bulk velocity $\widetilde{U}$, the freshwater depth $\widetilde{h}$, the gravitational acceleration $\widetilde{g}$ and the kinematic viscosity $\widetilde{\nu}$. With the density differences $\Delta\widetilde{\rho}_k$ and the mean density $\overline{\widetilde{\rho}}$, the reduced gravitational acceleration is defined as $\widetilde{g}'_k = \widetilde{g}\Delta\widetilde{\rho}_k/\overline{\widetilde{\rho}}$. Under the normalization $\min_\Omega\{c_k\} = 0$ and $\max_\Omega\{c_k\} = C_k = 1$, $x \in \Omega$, on the initial and boundary conditions, we define the Reynolds number as $Re = \widetilde{U}\widetilde{h}/\widetilde{\nu}$ and the Richardson numbers as $Ri_k = \widetilde{g}'_k\widetilde{h}/\widetilde{U}^2$.

With the dimensionless parameters $U = 1$, $h = 1$ and the function $f(x_2, x_3, t)) = [1 - \mathrm{erf}(\sqrt{\pi}(x_2 - 4h)/\delta)][1 + \mathrm{erf}(\sqrt{\pi}(x_3 - x_3^{\mathrm{in}}(t))/\delta)]/4$, where $\delta = h/40$ is the shear layer thickness, the inflow profile 'I' is specified as $u = \{Uf, 0, 0\}^\top$ for the velocity and $c_1 = C_1(1 - f)$, $c_2 = C_2 f$ for the concentrations, cf. Eq. (3). The vertical position of the interface, $x_3^{\mathrm{in}}(t)$, is described below in more detail. The outflow 'O' is modeled with boundary conditions (4) and $U_n = U$. Since the boundary conditions (4) successively wash the salt concentration out of the domain, we replace Eq. (4b) by $c_1 = C_1$, $c_2 = 0$ for $U_n^{\mathrm{g}} \leq 0$ and use additionally a sponge zone for the salinity to ensure that an appropriate and unique statistically stationary state for late times exists. For the fluid phase, the bottom 'B' is a no-slip and the top 'T' a non-deformable free-slip boundary. Accordingly, Eq. (4a) and (4b) are used in the vertical direction to model appropriate boundary conditions for the concentrations. To save computational effort, we introduce a symmetry plane at $y = 0$.

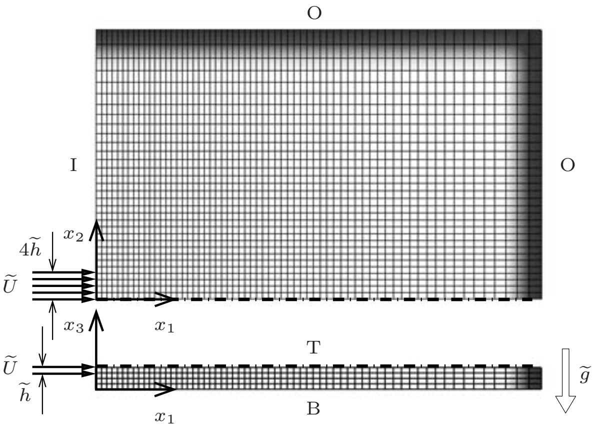

Figure 1: Simulation setup with the computational grid and the salt sponge (grey). Every 48th grid line is plotted.

Since we wish to have at least a qualitative comparison with the experiments of Maxworthy (1999), Parsons *et al.* (2001) and McCool and Parsons (2004), we try to comply with their physical parameters as far as possible. The Reynolds numbers in these experiments are on the order of 5 000 to 10 000 which is principally within reach for a time-dependent and accurate numerical simulation of the desired flow problem, e.g. by large-eddy (LES) or even direct numerical simulations (DNS). The Schmidt number Sc_1 of the salinity, however, is typically on the order of hundreds to thousands and the Schmidt number Sc_2 of discrete particles is even much larger, such that these values are far too large for a numerical simulation and need to be reduced in the simulation. Additionally, the ratio $\widetilde{u}_2^{\mathrm{s}}/\widetilde{U} = u_2^{\mathrm{s}}/U$ of the Stokes settling velocity and the freshwater bulk velocity is always smaller than 10^{-3} in the cited experiments. From numerical experiments we know that mainly this ratio governs the horizontal expansion of the particle plume and that such a small value would lead to very large horizontal extents L_1, L_2 of the domain. Hence, we have to enlarge the Stokes settling velocity in our numerical setup. Summing up, we have to find a compromise between the before mentioned characteristic numbers to allow a numerical solution by means of DNS in this configuration. From previous numerical experiments we know that our discretization predicts within about ten time units even small flow structures accurately if the grid Peclet number $Pe_{\Delta x} = \max_{\Omega,i}\{d\,u_i \Delta x_i\}$ with $d = Re\max\{1, Sc_k\}$ is roughly below eighty. Ultimately, we choose the spatial extents $\widetilde{L}_1 = 80\,\widetilde{h}$, $\widetilde{L}_2 = 50\,\widetilde{h}$, $\widetilde{L}_3 = 4\,\widetilde{h}$ together with a Stokes settling velocity of $\widetilde{u}_2^{\mathrm{s}} = 0.02\,\widetilde{U}$ for the sediment and $\widetilde{u}_1^{\mathrm{s}} = 0$ for the salt concentration. With a spatial resolution of $N_1 \times N_2 \times N_3 = 2\,305 \times 1\,153 \times 193$ grid points and a moderate grid stretching in the horizontal directions (cf. Figure 1) we assume a Reynolds number of $Re = 1\,500$ which should be sufficiently large to admit also some shear-induced turbulence. The Schmidt numbers are reduced to $Sc_1 = 1$ and $Sc_2 = 2$ to account at least for the difference in the diffusivities of salinity and particles which is required e.g. for double-diffusive sedimentation (Parsons *et al.*, 2001).

The salinity Richardson number Ri_1 basically determines if the inflow is sub- or supercritical, i.e. if a hydraulic jump occurs behind the inflow or not. In our configuration we would consider such a hydraulic jump as unphysical, since the saltwater in a real experiment would try to leave the domain via the fresh water inflow, i.e. the hydraulic jump would be retained in the domain only due to the “fixed” inflow boundary condition. On the other hand, strongly supercritical inflows are untypical in nature and occur mainly if no stabilizing salinity and/or temperature gradients are present. If we neglect the suspended particles, then incompressible, inviscid flows with a sharp interface are considered as supercritical if $Ri_1 < 1$ which indicates that disturbances cannot move upstream. On the other hand, we know from Bernoulli’s theorem that for $Ri_1 = 1/2$ the kinetic energy of the freshwater inflow balances exactly the potential energy of the salinity in the case of a potential flow. Because we have no better a priori estimate at hand, we simply choose the lower value $Ri_1 = 1/2$ such that we expect a slightly supercritical inflow. As a side effect, this value for Ri_1 feeds more kinetic energy into the domain compared to the critical value which promotes convective mixing in the domain additionally. The relative density difference $\Delta\widetilde{\rho}_1/\overline{\widetilde{\rho}}$ between freshwater and seawater is typically 0.005 to 0.02 near the continental shelfs, whereas the contribution of the suspended particles to the overall density is typically one order of magnitude below these values. Accordingly, we assume $Ri_2 = 0.1 Ri_1$ in our simulations.

From a linear stability analysis of the inflow profile at $x_2 = 0$ we find that it is unstable. Practically, however, the rather high viscosity plays a significant role in this context since it spreads the interface profile downstream rapidly and diminishes the growth rates strongly. Hence, we excite the instability of the shear flow additionally by introducing small disturbances, or more specifically, by simply moving the vertical position of the interface $x_3^{\mathrm{in}}(t) = x_3^0 + x_3^{\mathrm{rand}}(t)$ randomly around the average position $x_3^0 = L_3 - h$. The random contribution is derived for each grid plane in the x_2-direction separately from a so-called Ornstein–Uhlenbeck process with the reference time $T_{\mathrm{rand}} = 1000$ and variance $\mathrm{var}[x_3^{\mathrm{rand}}] = (0.005h)^2$.

The initial conditions for the velocity and the salt concentration in all x_2-x_3 planes along the x_1 coordinate are identical to the inflow boundary condition with $x_3^{\mathrm{rand}}(0) = 0$. The influence of the salinity dominates over the effect of the particles due to the large difference between the Richardson numbers such that the freshwater flow is mostly influenced by the salinity. Because we are mainly interested in the particle settling mechanism, we initiate the sediment concentration at $t = 250$, when the initial transient of the pure freshwater/saltwater interaction has mostly been washed out of the domain.

INTERACTION OF FRESHWATER AND AMBIENT SALTWATER

First, we investigate the interaction of the freshwater inflow and the ambient saltwater. Generally, basic two-dimensional Kelvin-Helmholtz (KH) waves are present up to $x_1 \approx 20\,h$, cf. Figure 2. It was already observed by Henniger and Kleiser (2008) that these “cat eyes” are pulled deeper below the water surface in this area. As a result, the increasingly unstable stratification causes a quicker vortex breakdown and the mixing of the freshwater with the ambient saltwater is correspondingly more effective. This effect is less pronounced in the present simulation since our salinity Richardson number is larger and the observation holds only for the central area of the estuary mouth near the symmetry plane. The mixing of fresh and saltwater in all other areas is obviously much less dominated by turbulence. Holmboe waves, that were observed in the experiments of McCool and Parsons (2004), do not apprear, probably because our inflow profile favors KH instability.

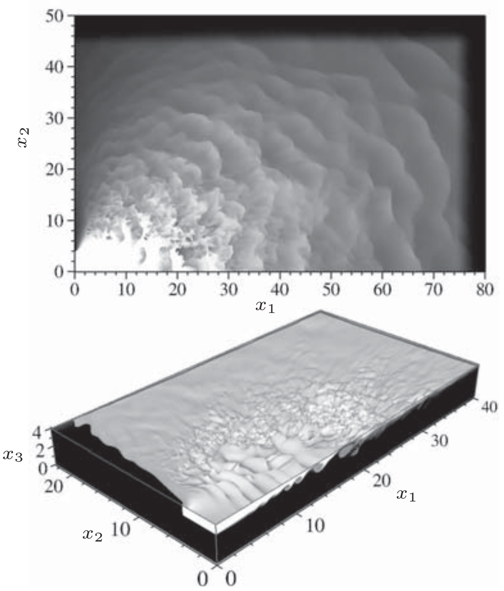

Figure 2: Salt concentration at $t = 250$. White: $c_1 = 0$, black: $c_1 = C_1$. Top: contour plot of $x_3 = L_3$ with sponge zone, bottom: isopycnal surface ($c_1 = 0.75\,C_1$) around the freshwater inflow.

The excitation of the inflow is purely random in order to trigger all disturbance wavelengths. Since the base profile varies in time and space, it is hard to find an a priori estimate for the largest growth rates or wave numbers of these disturbances. Practically, we only track internal waves by observing exemplarily their temporal and spatial evolution in the symmetry plane $x_2 = 0$. For this purpose it is convenient to evaluate the local potential energy of the salinity concentration at each point in this plane,

$$E_1^{\mathrm{pot,1D}} = Ri_1 \int c_1 x_3 \mathrm{d}x_3 \qquad (5)$$

From a plot of $E_1^{\mathrm{pot,1D}}$ with respect to x_1 and t (Figure 3) we find that the propagation of the internal breaking KH waves near the inflow is only slightly smaller than half of the freshwater bulk velocity U. This result is not surprising since the KH vortices have to act as a “ball bearing” between the fast freshwater layer and the standing brine underneath. The wavelengths as well as the vertical extents of these vortices are roughly equal to h such that their temporal frequency is slightly smaller than $0.5\,U/h$. The internal waves directly behind the breakdown area ($x_1 > 20\,h$) are not of KH type and travel obviously faster than the KH vortices at a speed closer to U. However, the propagation speed decreases with increasing distance to the inflow due to the decreasing speed of the freshwater current which is described below in more

Contents Main

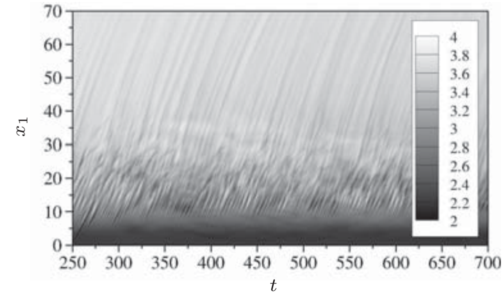

Figure 3: x_1-t diagram of $E_1^{\mathrm{pot,1D}}$ in the $x_2 = 0$ plane.

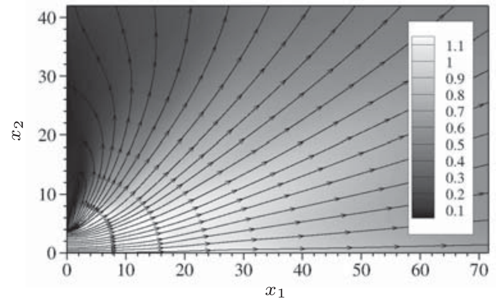

Figure 4: Mean absolute velocity $|\langle u\rangle|$ and streamlines of $\langle u\rangle$, $400 \leq t \leq 700$.

detail.

To further investigate the flow, we switch from time-dependent to time-averaged quantities $\langle\cdot\rangle \equiv \langle\cdot\rangle_{400\leq t\leq 700}$. The mean absolute velocity $|\langle u\rangle|$ as well as the streamlines based on $\langle u\rangle$ are depicted in Figure 4. The far-field of the averaged flow is obviously somewhat similar to that of a source in potential flow. Moreover, the mean absolute velocity drops from 1.0 directly at the inflow to about 0.5 in the far-field where it continues to decay only slowly further downstream. Though we did not establish an explicit inflow boundary condition for ambient saltwater at the outflow, also a considerable backflow beneath the freshwater/saltwater interface towards the freshwater inflow boundary can be observed (not shown here). This effect vanishes as soon as the suspended particles start to settle such that the backflow is effectively disturbed.

More information on the average flow is gained by the local freshwater bulk Richardson number Ri_{b} which we define in this context as

$$Ri_{\mathrm{b}} = \frac{Ri_1 \langle\Delta c_1\rangle \overline{h}}{|\langle\Delta u\rangle|^2} = \frac{Ri_1 \int (C_1 - \langle c_1\rangle)(L_3 - x_3)\mathrm{d}x_3}{\frac{1}{2}\int (\langle u_1\rangle^2 + \langle u_2\rangle^2 + \langle u_3\rangle^2)\mathrm{d}x_3} \qquad (6)$$

where $\langle\Delta c_1\rangle$ is a mean concentration difference, $|\langle\Delta u\rangle|$ a mean absolute velocity difference in the vertical direction and $\overline{h}$ a measure for the local depth of the freshwater current. Since the first expression is difficult to evaluate in practice, we rather stick to the definition of the Richardson number by relating the kinetic energy to an appropriate measure of the potential energy. Ri_{b} is evaluated at each point in the horizontal directions x_1, x_2, as depicted in Figure 5. Downstream of (but still near to) the freshwater inflow, it stays close to 0.5 since no hydraulic jump occurs, i.e. the flow is still critical or supercritical in this area. However, this is not the case for the wake besides the inflow where no momentum is available to counteract the salinity. In the area where the KH vortices saturate and finally break down, the flow is strongly time-dependent and nonlinear. The bulk Richardson number is slightly larger than one, however, this observation is not further investigated in more detail at this point since it might be only an artifact of our definition of Ri_{b}. In the remaining areas further downstream the bulk Richardson number lies again between about 0.5 and 1.0 which suggests that the flow tries to remain critical, i.e. $|\langle u\rangle|^2 \sim \overline{h}$.

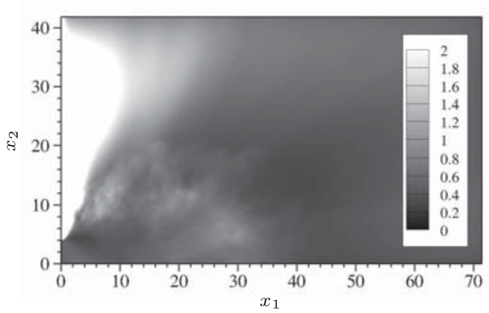

Figure 5: Mean bulk Richardson number Ri_{b}, $400 \leq t \leq 700$.

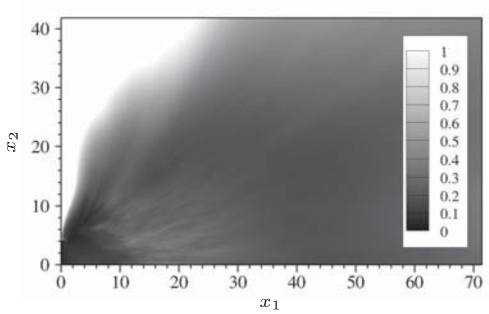

Figure 6: Mean gradient Richardson number Ri_{g}, $400 \leq t \leq 700$.

To detect whether disturbances grow or decay in our flow, we define the gradient Richardson number as

$$Ri_{\mathrm{g}} = \frac{-Ri_1 \min_{x_3}\left\{\frac{\partial\langle c_1\rangle}{\partial x_3}\right\}}{\max_{x_3}\left\{\left(\frac{\partial\langle u_1\rangle}{\partial x_3}\right)^2 + \left(\frac{\partial\langle u_2\rangle}{\partial x_3}\right)^2 + \left(\frac{\partial\langle u_3\rangle}{\partial x_3}\right)^2\right\}} \qquad (7)$$

It is evaluated for each point in the x_1-x_2 plane separately and plotted in Figure 6. The inflow region immediately before the KH vortices saturate must be fully unstable since Ri_{g} is much smaller than the analytical threshold 1/4 for inviscid flows and the triggered disturbances actually grow downstream. Behind the KH breakdown region, Ri_{g} stays slightly above the critical value of 1/4 which coincides with the experimental observations of McCool and Parsons (2004). This result is also supported by the observation that no growing disturbances can be observed in that area.

PARTICLE TRANSPORT AND PARTICLE SETTLING

After continuously adding the particle suspension to the inflowing freshwater, beginning at $t = 250$, the particle concentration is first transported more or less passively with the carrier fluid close to the inflow. As soon as the particles have travelled beyond the KH vortex breakdown, their transport speed decelerates due to the spreading of the freshwater current. Consequently, also the density difference, the diffusion and the Stokes settling velocity of the particle concentration play a more significant role outside the turbulent areas, which promotes an enhanced convective particle settling. As mentioned in the beginning, we are particularly interested in the settling mode of the particles. For this purpose we visualize two slices exemplary through the domain at $x_2 = 3$ (Figure 7) and at $x_1 = 26$ (Figure 8). From these

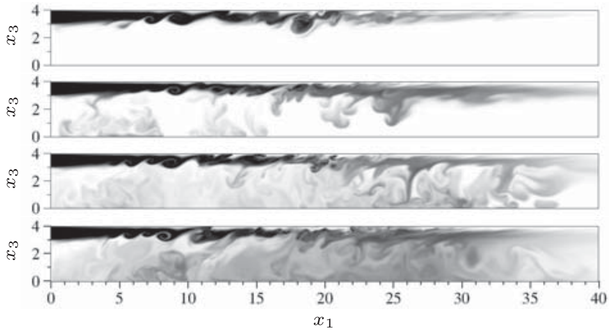

Figure 7: Particle concentration in the plane $x_2 = 3$. White: $c_2 = 0$, black: $c_2 = C_2$. From top: $t = 300$, 350, 400, 600.

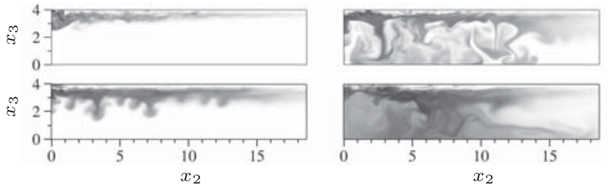

Figure 8: Particle concentration in the plane $x_1 = 26$. White: $c_2 = 0$, black: $c_2 = C_2$. Left column $t = 300$, 350, right column $t = 400$, 600.

pictures, one can easily observe a finger-like settling convection at early times which could be categorized somewhere between "mixing convection" in the experiments of Maxworthy (1999) and "finger convection" in the experiments of Parsons *et al.* (2001). The fingers are initially more or less two-dimensional as shown in Figure 9 where the particle concentration is seen from below. Moreover, the finger structures are aligned with the direction of the streamlines, cf. Figure 4. Finger convection is in principle sensitive to shear, such that these structures are obviously an effective way for the particles to overcome the influence of the shear stresses. However, this settling mode is accentuated only around $t \approx 350$. At later times, the settling becomes increasingly disordered and isotropic.

Since individual particles cannot be traced in our Eulerian description, we define the *effective* settling velocity

$$u_2^{\mathrm{s,eff}} = \int c_2(u_3 - u_2^{\mathrm{s}})\mathrm{d}V / \int c_2 \mathrm{d}V \qquad (8)$$

to investigate the particle settling speed. However, the different regimes in the physical domain contribute differently to this mean value. For instance, the particles in the inflow region are convected mainly in the horizontal directions whereas the vertical movement is neglegible. Figures 7 and 8 suggest that the effective settling velocity near the free surface is only slightly increased in contrast to the region below the freshwater/saltwater interface. Two evaluations of Eq. (8) with $x_3 \in [0, L_3]$ and $x_3 \in [0, L_3 - h]$ are plotted in Figure 10. As supposed, only the latter interval displays a significant increase of the effective settling velocity which is about $u_2^{\mathrm{s,eff}} \approx 1.4\, u_2^{\mathrm{s}}$ with respect to the Stokes settling speed.

The total mass of suspended particles in the domain

$$m_2 = Ri_2 \int c_2 \mathrm{d}V \qquad (9)$$

starts to decelerate at about $t = 320$, i.e. as soon as the fingers touch the ground, cf. Figure 11. At about $t = 550$, the sediment mass in the control volume is more or less saturated. Similarly, the integral mass flux over the boundaries

$$\Delta \dot{m}_2 = Ri_2 \oint c_2(u + u_2^{\mathrm{s}} e^{\mathrm{g}}) \cdot n \, \mathrm{d}A \qquad (10)$$

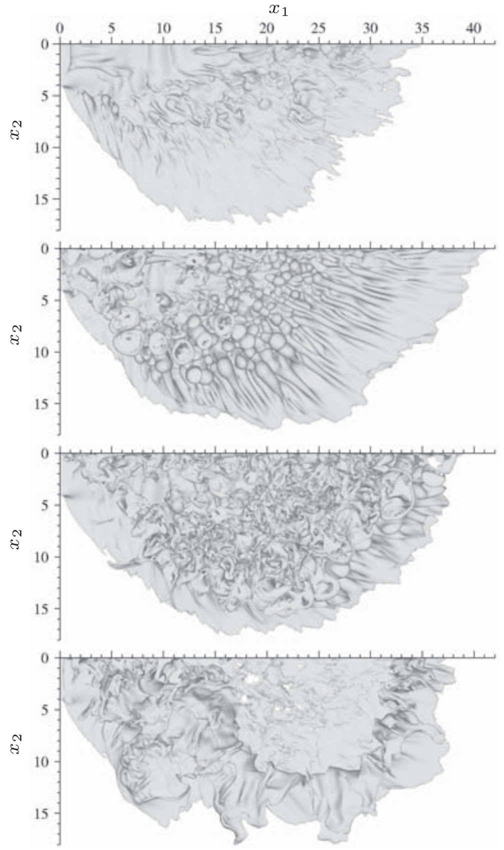

Figure 9: Isopycnal layer ($c_2 = 0.1\, C_2$, view from below) of the particle concentration. From top: $t = 300$, 350, 400, 600.

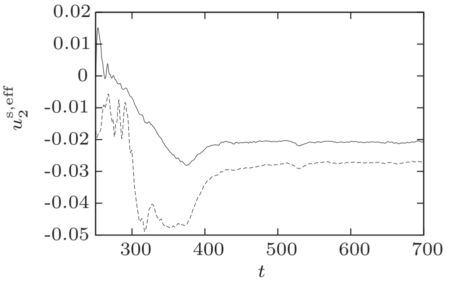

Figure 10: Effective particle settling velocity over time. Vertical integration interval $x_3 \in [0, L_3]$ (solid line), $x_3 \in [0, L_3 - h]$ (dashed line).

drops from initially $4Ri_2C_2Uh^2$ to approximately zero as depicted in Figure 11. The settling convection is mostly driven by the available kinetic energy of the inflow and the potential energy

$$E_2^{\mathrm{pot}} = Ri_2 \int c_2 x_3 \mathrm{d}V \qquad (11)$$

of the particles. However, not all of the potential energy is available, such that the *available* potential energy (Peltier and Caulfield, 2003),

$$E_2^{\mathrm{pot,avail}} = E_2^{\mathrm{pot}} - Ri_2 L_1 L_2 \int c(x_3^*) x_3^* \mathrm{d}x_3^* \qquad (12)$$

is of more interest since only this amount of energy can essentially be transformed into kinetic energy, for instance. The integral in Eq. (12) represents the minimum potential energy ("background potential energy") which is attainable through adiabatic restratification of the fluid (see e.g. Peltier

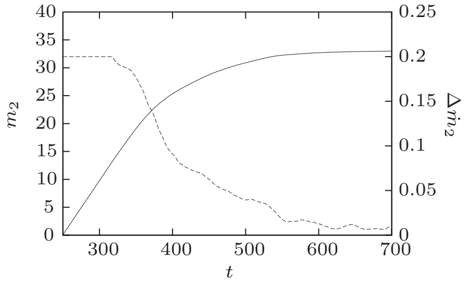

Figure 11: Sediment mass (solid line) and sediment mass flux imbalance (dashed line) over time.

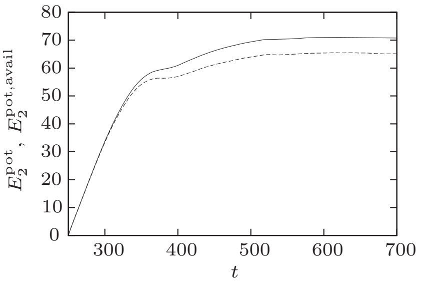

Figure 12: Absolute potential energy (solid line) and available potential energy (dashed line) of sediment over time.

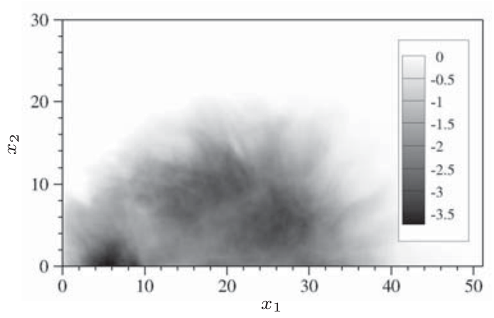

Figure 13: Deposit distribution at $t = 700$.

and Caulfield (2003) for more details). The restratification can be easily performed in a statistical manner by means of a histogram for the concentration that can be integrated subsequently over the vertical coordinate x_3^*. From Figure 12 we find that both energies coincide until the sediment concentration touches the ground for the first time. Beyond that point the available potential energy is smaller than the total potential energy since a distinct portion of particles on the ground cannot contribute to convective motion anymore.

Finally, the deposit distribution of the sediment on the ground,

$$D = \int c(x_3 = 0) u_2^{\mathrm{s}} \mathrm{d}t \qquad (13)$$

is evaluated in Figure 13. Mainly two different observations can be made: first, most of the deposit is located in a thick semicircular band around the freshwater inflow where it is rather evenly distributed. Second, directly in front of the inflow and within the semicircular area is the largest amount of deposit per area. Whereas the first part of the sediment is the result of the convective particle settling behind the KH vortex breakdown area, the latter is caused by a convective particle settling directly from the area of the supercritical inflow which is also visible in Figure 7. Hence, this separation of the particle phase can be regarded as a “divergence” of the particle concentration on its way to the ground. Such phenomena are also assumed to occur in nature (Parsons *et al.*, 2001).

CONCLUSION AND OUTLOOK

We presented a numerical simulation setup and results of an laboratory-scale estuary flow. The results demonstrate that the simulation of such a configuration is generally feasible, under the restriction that certain parameters, such as the large Schmidt numbers, cannot be represented correctly. Other parameters, such as the Richardson numbers or the inflow profile, are not unique for all estuaries and can be specified with only few restrictions.

Especially the Schmidt numbers can play a significant role in the initiation of an enhanced convective particle settling. However, the results show that the basic settling mechanisms of the experiments of Maxworthy (1999), Parsons *et al.* (2001) and McCool and Parsons (2004) are still well rendered by the simulation, possibly because we maintain a certain ratio between the Schmidt numbers of the particle suspension and the salinity. In either case, the effective particle settling speed compared to the Stokes settling velocity is similarly enhanced as in actual measurements.

We plan to conduct further simulations with different parameter values in the future. Besides the influence of the too small Schmidt numbers, also that of the Stokes particle settling speed needs to be further investigated. Other environmental influences, such as temperature differences or Coriolis forces, could be taken into account as well.

ACKNOWLEDGMENTS

Rolf Henniger would like to thank Eckart Meiburg for making possible a stay at UCSB during fall 2008. Support has been obtained through the ETH research grant TH-23/05-2. All computations were performed at the Swiss National Supercomputing Centre (CSCS).

REFERENCES

Henniger, R., Kleiser, L., 2008, “Simulation of Gravity-Driven Flows Using an Iterative High-Order Accurate Navier–Stokes Solver”, *Direct and Large-Eddy Simulation VII*, to appear.

Henniger, R., Obrist D., Kleiser, L., 2007, “High-Order Accurate Iterative Solution of the Navier–Stokes Equations for Incompressible Flows”, *Proc. Appl. Math. Mech.*, Vol. 7, pp. 4100009–4100010.

Henniger, R., Obrist D., Kleiser, L., 2009, “High-Order Accurate Solution of the Navier–Stokes Equations on Massively Parallel Computers”, submitted.

Maxworthy T., 1999, “The Dynamics of Sedimenting Surface Gravity Currents”, *J. Fluid Mech.*, Vol. 392, pp. 27–44.

McCool W. W., Parsons J. D., 2004, “Sedimentation from Buoyant Fine-Grained Suspensions”, *Cont. Shelf Res.*, Vol. 24, pp. 1129–1142.

Parsons, J. D., Bush, J. W. M., Syvitski, J. P. M., 2001, “Hyperpycnal Plume Formation from Riverine Outflows with Small Sediment Concentrations”, *Sedimentology*, Vol. 48, pp. 465–478.

Peltier W. R., Caulfield C. P., 2003, “Mixing Efficiency in Stratified Shear Flows”, *Annu. Rev. Fluid Mech.*, Vol. 35, pp. 135–167.